Unravelling phononic, opto-acoustic and mechanical properties of metals with light-driven hypersound

Hao Zhang,[1,2,*] Alessandro Antoncecchi,[1,2] Stephen Edward,[1,3]
Irwan Setija,[4] Paul Planken,[1,3] and Stefan Witte[1,2,†]

[1] *Advanced Research Center for Nanolithography, Science Park 106, 1098 XG Amsterdam, the Netherlands*
[2] *Vrije Universiteit Amsterdam, De Boelelaan 1105, 1081 HV, Amsterdam, the Netherlands*
[3] *Universiteit van Amsterdam, Science Park 904, 1098 XH Amsterdam, the Netherlands*
[4] *ASML Research, De Run 6501, 5504 DR Veldhoven, the Netherlands*

A thorough understanding of the electron-phonon, thermo-optic and acoustic properties of materials is of paramount importance for many applications in materials science and advanced applications adopting laser-induced sound waves. Even though metals are usually opaque to light, optical methods for materials characterization can still be developed, especially in the high-frequency regime where phonon dynamics governs the thermal, acoustic and even optical properties of metals. Ultrafast laser pulses incident on metals can lead to the generation of coherent phonon wave packets with frequencies in the gigahertz to terahertz range, providing a means to study material properties in this otherwise inaccessible frequency range. While this principle has been known, the complex interplay of light and matter in both the generation and detection of such ultrafast hypersound pulses has limited its use mainly to geometrical effects. Here we demonstrate the quantitative characterization of a range of different material properties using laser-driven hypersound. We use all-optical generation and detection of hypersound pulses to sensitively probe the bulk properties of various metals. We introduce an advanced 2D numerical model that captures generation, propagation and detection of these hypersound waves in full detail. The combination of experiment and simulation allows us to unravel and elucidate various physical effects that appear over a wide range of different timescales. Through least-squares fitting of the data to the simulation results, we extract quantitative information about electron-phonon, thermo-optic and acoustic properties of metal films, establishing the ability to use light as a sensitive probe for the study of opaque materials.

I. INTRODUCTION

The microscopic structural and electronic properties of solids are influenced by a wealth of complex physical phenomena. A thorough understanding of complex solids, such as phononic structures [1–4] and functional nanostructures [5], requires a means to probe such dynamics of both surface and bulk properties in a non-invasive way. While pump-probe studies using ultrashort light pulses are a proven method for time-resolved measurements, a large range of condensed media are opaque to visible and near-infrared light, hampering the use of such optical techniques to study bulk material properties. Nevertheless, methods to study bulk materials have been developed, based on the use of laser-induced acoustic waves that can penetrate into optically opaque media [6, 7]. Ultrafast laser pulses incident on absorptive solids can lead to the generation of coherent phonon wave packets with frequencies in the gigahertz (GHz) to terahertz (THz) range. Such a high acoustic frequency range, also known as hypersound [1], is suitable to probe the phonon spectrum of most materials, and goes well beyond the capabilities of conventional acoustic measurements based on transducers. This approach, also known as picosecond ultrasonics, has become a powerful tool for nanometer-scale thin-film metrology in the semiconductor industry [8]. The corresponding acoustic wavelength can be as short as few nanometers, which has motivated research on acoustic imaging of buried-nanostructures beyond the optical diffraction limit [9, 10]. Picosecond ultrasonics has led to fundamental studies concerning electron diffusion and electron-phonon coupling in metals [11–13], interband transitions [14, 15], nonlinear acoustics and soliton [16–19], magnetoacoustics [20], acoustic focusing and shock waves [21, 22], and hypersound damping mechanisms [23–26].

The concept of picosecond ultrasonics experiments [6, 7, 27] can be summarised as follows, also shown in Fig. 1. An ultrafast pump laser pulse first excites the sample surface, giving rise to an elevated temperature of the electron gas. The energetic electrons thermalize with the lattice which is initially cold, until a common temperature is reached. The rapid increase of lattice temperature causes an abrupt expansion of the sample top layer, which leads to the generation of a strain pulse whose spatial extent and frequency are determined by both the electron-phonon coupling strength and the electron transport and thermal diffusion. For strongly absorbing metals with high electron-phonon coupling, the energy transfer to the lattice is confined to a depth of a few nanometers, leading to a high frequency, longitudinal acoustic pulse that propagates into the sample at the speed of sound. For sufficiently large excitation energy, nonlinear acoustic waves and even solitons have also been observed [17, 19, 28]. Spatial inhomogeneity of either the excitation profile or the illuminated surface

* H.Zhang@arcnl.nl
† S.Witte@arcnl.nl

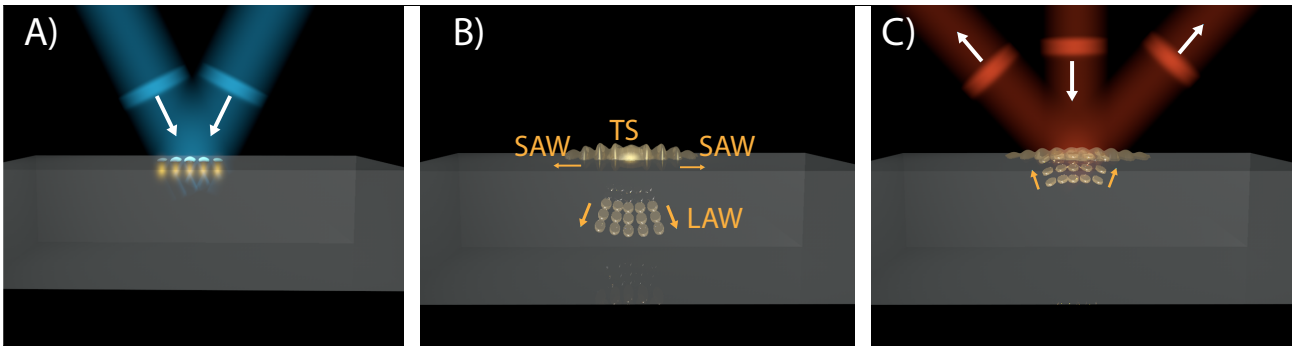

FIG. 1. Schematic of laser-induced hypersound experiments. A) An ultrafast laser pulse (here depicted as a transient grating, where two pulses interfere at the sample surface), heats the electrons in a thin layer at the surface of an opaque medium (here shown partially transparent for viewing purposes). B) The electron energy is transferred to the lattice, resulting in ultrahigh-frequency acoustic phonons that travel into the sample as longitudnal acoustic waves (LAWs) or along the surface as surface acoustic waves (SAWs). A local temperature increase at the surface also results in thermal stress (TS). C) The returning LAWs, as well as the SAWs and TS lead to surface displacement and refractive index changes at the surface, which are detected with a delayed probe pulse through e.g. induced diffraction.

results in the excitation of shear waves and surface acoustic waves (SAWs) [29–33] or guided modes such as Lamb waves [34]. The generated acoustic pulse, when being reflected at a material interface inside a sample, appears as an echo propagating back to the sample surface. This echo, manifesting itself as atomic displacements and/or a local modification of the dielectric constant, can be detected optically by a delayed probe pulse through reflection [14], diffraction [30, 35] or interferometric measurements [19, 36].

However, while such hypersound experiments have enabled measurements of sample geometry, the quantitative retrieval of bulk material properties in such experiments has remained an open challenge. Various results on model-based analysis of experimental measurements have been reported [6, 12–15, 19, 20, 33, 35–38], which yielded remarkable results about the acoustic wave generation mechanism itself. Nevertheless, most of the models are based on a one-dimensional description of the acoustic wave propagation and only incorporate a rather limited description of the various physical effects in laser-induced hypersound. Due to this incompleteness in the existing models, to the best of our knowledge a rigorous, quantitative analysis of the experimental results through direct model fitting has not yet been achieved. Such a quantitative analysis is challenging yet demanding as it requires a comprehensive and yet accurate modelling of the complex interplay between all the different physical effects involved in the generation, propagation and detection of the hypersound pulses, which occurs over timescales that span orders of magnitude. The detected signal is a coherent addition of signals resulting from atomic displacements, strain- and thermo-optic effects, and possibly multilayer interference effects such as Brillouin scattering, and these signals in turn result from a combination of electronic and thermal effects, surface and longitudinal acoustic waves, possibly including multiple reflections from sub-surface interfaces. To disentangle all these different possible contributions and elucidate their respective roles in the signal formation, a full theoretical treatment should accompany the experiments. Fitting the experimental results to the output of such a model then enables a detailed analysis of the different physical effects involved, but also allow the retrieval of fundamental material properties such as electron-phonon coupling strengths, acoustic parameters, as well as acousto-optic and thermo-optic couplings [13, 35]. In addition, models based on a 1D wave equation [14, 20, 35–39], do not capture dynamics of surface acoustic waves (SAWs) and diffraction. These effects become important especially for nanoscale materials [29, 40] and structured or small excitation volumes [30, 33, 35, 38]. To include phenomena such SAWs and acoustic diffraction, a two-dimensional model is a minimum requirement. Furthermore, acoustic damping is an important but complex phenomenon at hypersound frequencies, as picosecond-timescale phonon dynamics can significantly influence microscopic viscosity and strain [24, 25, 41, 42]. Yet, these effects are usually not being considered.

In this paper we introduce a two-dimensional model that fully captures the above mentioned physics and nanoscale interactions of laser-driven hypersound in solids. We use this model in combination with ultrafast time-resolved experiments to characterize the propagation of hypersound in various thin films, and to retrieve information on a multitude of material properties that govern dynamics on timescales ranging from femto- to nanoseconds. The model equations are efficiently solved by a self-developed numerical code adopting 2-dimensional Finite-Difference Time-Domain (2D-FDTD) method, enabling least-squares fitting of the experimental data to the model simulations and thus a quantitative extraction of multiple electronic, thermo-optic and acoustic parameters of the investigated materials. In addition, we show that this combined approach enables disentanglement of various contributions to the

signal formation, including longitudinal and shear waves, SAWs, Lamb waves, acoustic diffraction, thermo-optic effect, Brillouin scattering and frequency-dependent damping and dispersion of the hypersound waves. The model has already found successful application in disentangling various physical effects and understanding signal formations in pump-probe sub-surface alignment metrology in photolithography [43].

II. NUMERICAL AND EXPERIMENTAL APPROACHES

A. Simulation of ultrafast photo-acoustics

The first step of the model is the absorption of the laser pulse and the generation of thermal stress due to the sudden heating of the lattice. The optical intensity inside the sample is calculated by solving the Maxwell's equations using the material permittivity and laser parameters as input. The energy transfer between the electrons and lattices is modeled via the two-temperature model [44], assuming separate temperatures for the electron and lattice subsystems [45, 46], and including energy transport through electron and phonon dynamics. The temperature dependence of electron heat capacity and thermal conductivity are also taken into account. More details on this first step can be found in the Supplemental Material [47].

In metals, thermoelasticity is the dominant mechanism for picosecond acoustic pulse generation [6, 12]. The elevation of the lattice temperature causes an isotropic thermal stress $\boldsymbol{\sigma}^{th}$ whose two cartesian components are given by

$$\sigma_x^{th} = \sigma_y^{th} = -3B\beta\Delta T_l(x,y,t), \tag{1}$$

where B is the bulk modulus and β is the linear expansion coefficient. The temperature increase $\Delta T_l(x,y,t)$ is obtained by the solution of the two-temperature model. Throughout this paper, the coordinate x represents the axis perpendicular to the sample surface while y is the axis along the surface.

To model the propagation of the sound waves, Eq. 1 is used as a source term in the equation of motion for an isotropic, linear elastic wave [48, 49]. The acoustic attenuation is introduced (additional relaxation effects will be introduced later) by adding two extra viscous terms as it is done in the Navier-Stokes equation [41, 50], resulting in the following equation of motion:

$$\rho\frac{\partial^2\mathbf{u}}{\partial t^2} = \mu\nabla^2\mathbf{u} + (\mu+\lambda)\nabla(\nabla\cdot\mathbf{u}) + \nabla\boldsymbol{\sigma}^{th} + \xi\nabla^2\mathbf{v} + (\xi+\lambda_v)\nabla(\nabla\cdot\mathbf{v}), \tag{2}$$

where $\mathbf{u}$ is the displacement vector, ρ the mass density, λ and μ are the two Lamé parameters, $\mathbf{v}$ is the velocity vector, ξ the coefficient of shear viscosity and λ_v is linked to the coefficient of bulk viscosity η as $\lambda_v = \eta - 2\xi/3$.

Expanding Eq. 2 in two-dimensional cartesian coordinate leads to two coupled differential equations for the velocity $\mathbf{v}$ and the strain field $\mathbf{s}$,

$$\frac{\partial v_x}{\partial t} = -\frac{1}{\rho}\left(\frac{\partial\sigma_x^{re}}{\partial x} + \frac{\partial\sigma_{xy}^{re}}{\partial y} + \frac{\partial\sigma_x^{v}}{\partial x} + \frac{\partial\sigma_{xy}^{v}}{\partial y} - \frac{\partial\sigma_x^{th}}{\partial x}\right),$$
$$\frac{\partial v_y}{\partial t} = -\frac{1}{\rho}\left(\frac{\partial\sigma_y^{re}}{\partial y} + \frac{\partial\sigma_{xy}^{re}}{\partial x} + \frac{\partial\sigma_y^{v}}{\partial y} + \frac{\partial\sigma_{xy}^{v}}{\partial x} - \frac{\partial\sigma_y^{th}}{\partial y}\right), \tag{3}$$

and,

$$\frac{\partial s_x}{\partial t} = \frac{\partial v_x}{\partial x};\quad \frac{\partial s_y}{\partial t} = \frac{\partial v_y}{\partial y};\quad \frac{\partial s_{xy}}{\partial t} = \frac{\partial v_x}{\partial y} + \frac{\partial v_y}{\partial x}. \tag{4}$$

In the above equations, s_x and s_y are the components of normal strain and s_{xy} the shear strain, σ_x^{re} and σ_y^{re} are the normal stresses and σ_{xy}^{re} is the shear stress. The superscript "re" stands for "restoring" as they originate from the restoring force. The strain field and the stress field are linked through the strain-stress relation, which can be obtained in the expansion of Eq. 2 as well:

$$\sigma_x^{re} = -(\lambda+2\mu)s_x - \lambda s_y;\quad \sigma_y^{re} = -(\lambda+2\mu)s_y - \lambda s_x,$$
$$\sigma_{xy}^{re} = -\mu s_{xy}. \tag{5}$$

The expansion of the attenuation terms in Eq. 2 leads to relations which link the viscous stresses to the strain rates:

$$\sigma_x^{v} = -(\lambda_v+2\xi)\frac{\partial s_x}{\partial t} - \lambda_v\frac{\partial s_y}{\partial t},$$
$$\sigma_y^{v} = -(\lambda_v+2\xi)\frac{\partial s_y}{\partial t} - \lambda_v\frac{\partial s_x}{\partial t},$$
$$\sigma_{xy}^{v} = -\xi\frac{\partial s_{xy}}{\partial t}. \tag{6}$$

It can be seen that the dynamics of velocity and strain fields (Eq.3 and Eq. 4) are coupled through Eq. 5 and Eq. 6. Here we observe that there is a close analogy to the Maxwell's equations, where the $\mathbf{E}$ field and the $\mathbf{B}$ field are coupled through the time and spatial derivatives, and the response of the media to the external field is described by the constitutive relation, which establishes the relation between the electric displacement field and the electric field. The constitutive relations in the present case of acoustic propagation are the strain-stress relation and Eq. 6. The above analogy implies that Eq. 2 can be solved by the FDTD method [51], which was originally developed for solving the time-dependent Maxwell's equations [52].

The third step of the model is to calculate the optical response of the material. In picosecond ultrasonics experiments, a delayed (probe) pulse is used to detect the response of the sample due to the pump pulse. This is usually realized by measuring the changes in sample reflectivity [14], diffraction efficiency in the case of transient grating experiments [30, 35], or interferometric measurements [19, 36] where the electric field amplitude and phase of the probe pulse are both measured. From a modelling point of view, all these quantities require a calculation of the (reflected) complex electric field of the

probe pulse in the presence of pump excitation. In general, the reflected electric field of the probe is affected by either surface displacement (which only influence the phase) or a local transient variation of the refractive index (which may influence both amplitude and phase) due to the presence of strain (strain-optic effect) or temperature elevation (thermo-optic effect). Using the outputs of the model in the previous steps, i.e., the lattice temperature, the strain field and the displacement field as a function of space and time, the reflected complex electric field can be calculated by numerically solving the Maxwell's equations for the probe pulse, providing that the strain-optic and thermo-optic coefficients are known. In this work we use the transfer-matrix method [53] to calculate the reflected field, and details are provided in the Supplemental Material [47].

B. Setup for hypersound generation and detection

A schematic of the experimental setup is shown in Fig. 2(a). Pulses from an amplified Ti:Sapphire system (Femtopower, Spectra Physics, duration 30 fs, central wavelength 800 nm, repetition rate 1 kHz) are split into pump and probe pulses by a 1% beam splitter. The stronger part is frequency doubled in a BBO crystal to 400 nm wavelength to be used as pump beam. This beam is subsequently split into two beams by a 50% beam splitter. The two pump beams are then loosely focused onto the sample at a slightly oblique angle ($\sim 2°$). The pump beam diameter on sample is estimated as ~ 1 mm. The pump pulse energy ranges from 3 μJ to 15 μJ depending on the sample used. Special care was taken to ensure overlap of the two pump pulses in space and time, creating interference fringes with a period of ~ 6 μm. The interference pattern excites the sample, leading to a spatially periodic heating of the sample surface and thus generating a spatially periodic array of acoustic pulses. This periodic array acts as a transient grating, propagates through the sample and internally reflects at material interfaces. A probe beam (800 nm) then illuminates the pumped surface, and its time delay with respect to the arrival of pump pulse is controlled via an optical delay line. This probe beam is then diffracted by the pump-induced change to the sample. The energy contained in the first-order diffraction is measured by a photodetector and the signals are subsequently sent through a box-car integrator and collected by a data acquisition card as a function of pump-probe delay. To improve detection accuracy, one of the pump beams passes through a 500 Hz mechanical chopper, so that the signal without pump excitation is also measured. This allows us to subtract the background level from the signal with pump excitation to ensure that only the pump induced change is measured. The data belonging to the same pump-probe delay is averaged over 100-500 pulses to further increase signal-to-noise level. More details about the setup can be found in Ref. [54].

Experimental data were obtained through measurements on either metal-film-on-substrate samples or free-standing metal membranes. Metals with a large difference in electron-phonon coupling strength (Au, Al and Ni) are chosen as electron-phonon coupling is the dominant factor determining the frequency of the excited sound waves. The use of free-standing membranes ensures that more acoustic echoes can be measured as reflection loss at interfaces is minimized, and metal-film-on-substrate samples are measured for comparison. Fig. 2(b) shows a typical transient diffraction efficiency signal measured on a 200-nm-Au-layer on glass substrate sample. The fast signal around zero time delay originates from the generation of hot electrons, which give rise to a change in the local dielectric function. This contribution vanishes after a few picoseconds as the energy is transferred to the lattice due to electron-phonon coupling. This abrupt heating of the lattice sets up a thermal stress which generates acoustic pulses at material boundaries. In fact, the temperature distribution obtained during the calculation shows that the whole layer is heated up almost homogenously thanks to the relative weak electron-phonon coupling of Au [55–58] combined with fast electron diffusion and ballistic range, compared with the relative thin film thickness. This near-homogenous heating generates two acoustic pulses launched almost at the same time, one starting at the Air/Au interface and the other starting at the Au/glass interface. The two acoustic pulses propagate in the opposite direction and reflect back and forth inside the Au layer, forming a "breathing-like" mode with a period determined by one round trip time of the acoustic pulses. These are recovered in the model calculation using electronic and mechanical properties of Au (Video1 in the Supplemental Material [47]).

C. Fitting experimental data

To quantitatively extract the material properties, measured signal (data of $t >$5–10 ps after the electron-phonon coupling) as a function of pump-probe delay is then normalized by the maximum value and least-squares fitted using the model described in section II A. Important electronic and acoustic properties of the metal layers such as electron-phonon coupling, speed of sound, acoustic attenuation, thermal-optic coefficient etc. and some experimental conditions with small uncertainties such as the transient grating period are treated as fitting parameters while other parameters are either taken from known literature values or estimated from experimental conditions. Least-squares fitting with multiple fitting parameters can be hindered by multiple local minima in the fitting residual. In order to obtain a solution as close as possible to the true global minima, we use a so called "multi-start" fitting procedure. We first randomly generate some 200–500 parameter values for each of the fitting parameters within predetermined intervals, forming 200-500 initial parameter sets. Least-squares fitting routines are then

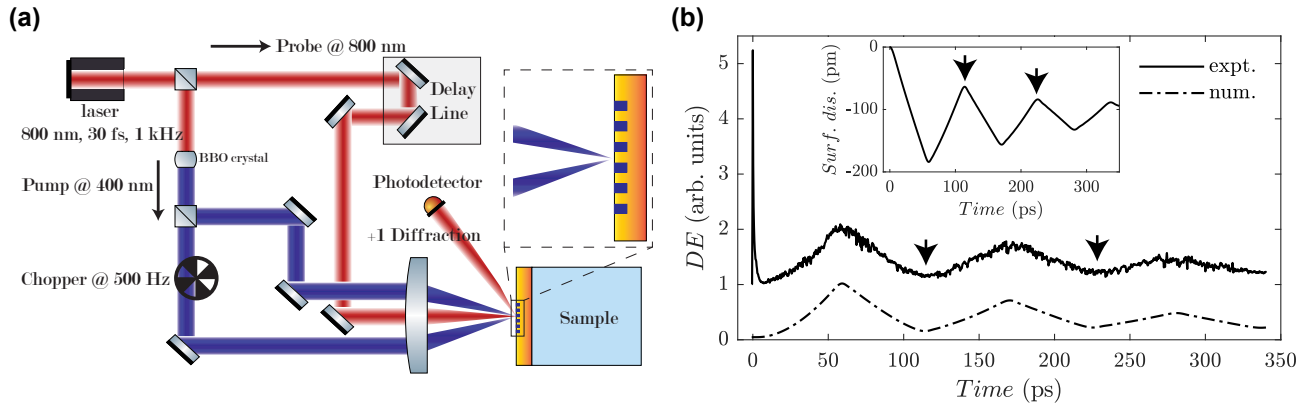

FIG. 2. (a) Schematic of the experimental setup. Two crossed pump beams are used to create interference fringes on the sample surface. (b) Typical diffraction efficiency (DE) measurement on a 200 nm Au film deposited on glass substrate and model calculation which well reproduces the measured acoustic response. The inset shows calculated surface displacement (in the direction perpendicular to the surface) at the center of the grating line. The arrows mark the returning of echoes. Note the experimental curve has been given an offset for clarity.

carried out separately using each of the parameter sets as initial guess values. This procedure generates 200-500 optimized parameter sets. Those parameter sets are then sorted by their normalized fitting residual, χ^2. The best-fit values are determined as being the set of parameters which yields the lowest residual, χ^2_{min}. The upper and lower bounds of fitted parameters are also determined from those optimized parameter sets using a predefined $\Delta\chi^2 = (\chi^2 - \chi^2_{min})/\chi^2_{min}$ criterion. More details about the fitting method are provided in the Supplemental Material [47].

III. RESULTS AND DISCUSSION

A. Hypersound characterization of a free-standing aluminium membrane

Experiments on Al were performed on a 400 nm free-standing membrane. In Fig. 3(a) we plot the measured data, along with the best-fit model calculation, and the resulting diffraction efficiencies calculated by only the total surface displacement and by only the thermo-optic effect. The measured signal is a coherent sum of the electric fields of the individual contributions, rather than a direct sum of diffraction efficiencies. The surface displacement contribution acts as a pure phase grating while the thermo-optic contribution acts as both amplitude and phase grating. The signal of the first 50 ps is dominated by the thermo-optic effect which manifests as a decaying background caused by heat diffusion, and therefore we also treat the thermal conductivity as a fitting parameter to better recover the background. The calculated temperature evolution is shown in Fig. 3(b). The contribution from surface displacement itself can be divided further into 3 sub-contributions, namely, from the thermal surface expansion (TSE, Fig. 3(f)), the longitudinal acoustic waves (LAWs), Fig. 3(f-h)), and the surface acoustic waves or more specifically, Lamb waves in free membranes(Fig. 3(i)). The TSE is caused by the temperature increase and decays slowly as the surface cools down, while the longitudinal acoustic wave is generated because of the rapid surface expansion. The longitudinal wave which reflects off at the other side of the membrane, when it returns to the surface region, contracts the TSE and therefore reduces the diffraction signal. This event happens every acoustic round-trip time, thus appearing as equally spaced dips in Fig. 3(a). These two contributions will be discussed further later in the discussion of the gold results: the difference is that we see a better separation of these two effects in the aluminum data because of a much shorter spatial extent of the excited acoustic pulse. This high frequency content results from aluminum's much higher electron-phonon coupling strength and slow electron thermal diffusion without ballistic transport. Another noteworthy observation is the overall increase of diffraction efficiency after $\sim$ 400 ps, which we believe is caused by an excitation of Lamb waves. This is further substantiated by running a simulation with a very high attenuation coefficient set for the longitudinal waves, so that the longitudinal echoes are damped out in the first few round-trips, leaving only the contributions from TSE and Lamb waves at longer time delays. The resulting model signal is shown by the dashed line in Fig. 3(a), in which we see the same increase in diffraction efficiency after 400 ps as the experimental measurement. In Fig. 3(c) we plot an extended calculation from only the TSE and Lamb waves, up to 20 ns (Also see Video3 in the Supplemental Material [47]). The result shows a periodic oscillation with a period of $\sim$ 10.6 ns. On top of this slow oscillation we also observe a smaller but faster oscillation with a period of $\sim$ 1 ns. This oscillatory signal is due to the interference of excited Lamb waves at the periodical boundary.

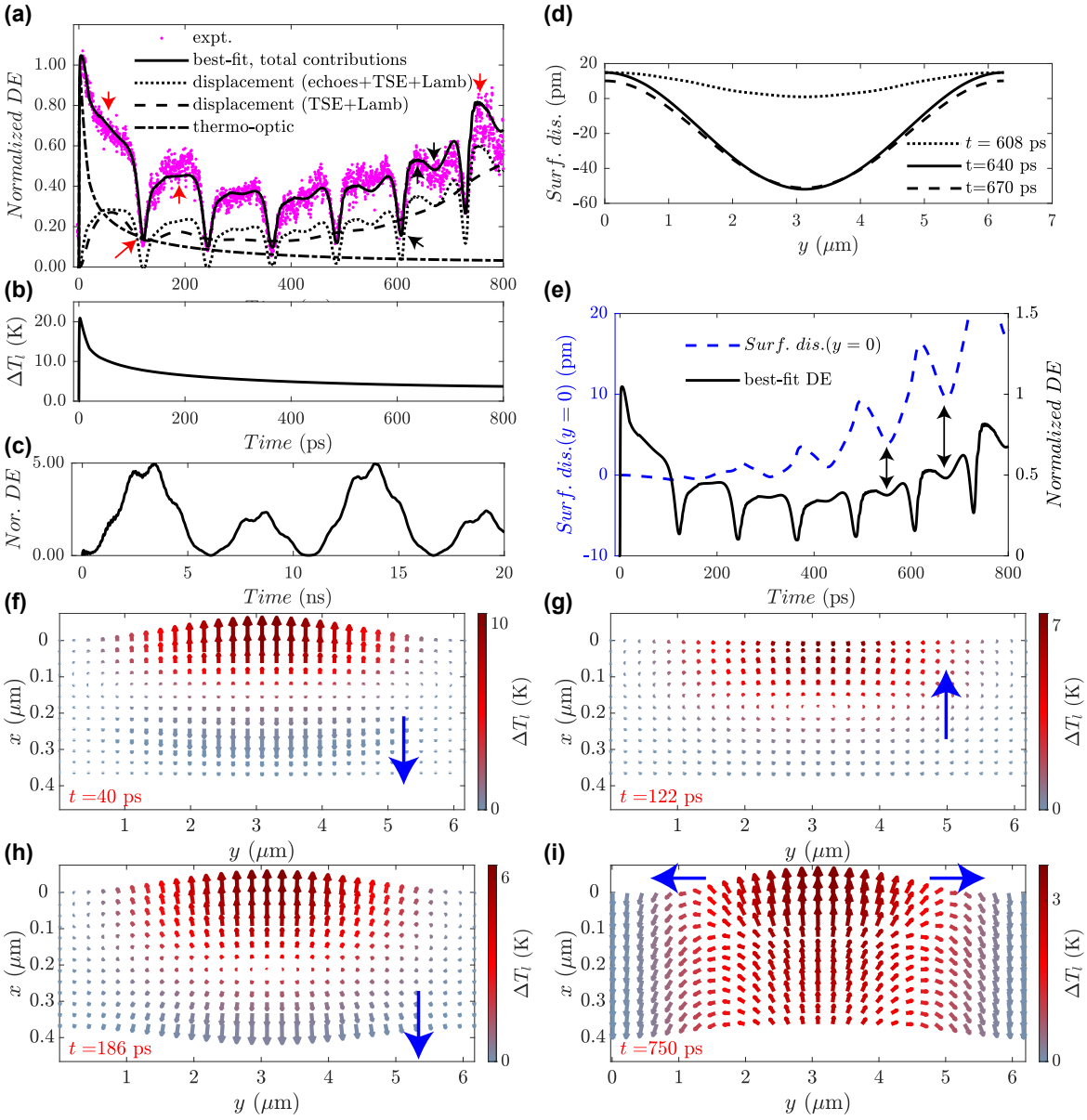

FIG. 3. (a) Measured diffraction efficiency (dots) and corresponding model fit (solid line) on a 400 nm Al free-standing membrane. The dotted line, dashed line, and dash-dotted line are diffraction efficiencies from each contributions: the total surface displacement, surface displacement of TSE and Lamb waves, and the thermo-optic effect. The increase of surface temperature at the center of grating line is shown in (b). Calculated diffraction efficiency (normalized) due to the interference of Lamb waves is shown in (c) for an extended period of time, illustrating its periodic nature. The normal component of the displacement vector along the sample surface is shown in (d) for 3 time instants which are marked by black arrows in (a). (e) Normal component of the surface displacement vector (blue dashed line) at the periodic boundary ($y = 0$). The double-side arrows mark the timing of the extra dips. The displacement vector distribution at 4 time instants (marked by red arrows in (a)) which illustrate (f) the generation of TSE and longitudinal acoustic wave, (g) contraction of the surface due to the returning of the longitudinal wave, (h) the recovery of the TSE, and (i) the appearance of Lamb waves at longer time delays. The color represents the increase in the lattice temperature. The blue arrows indicate the propagation direction of the longitudinal wave and Lamb waves. Note that the displacement vectors are highly exaggerated to be visible for solely illustrative purpose. Also see Video2 and Video 3 in the Supplemental Material [47].

These two frequencies (~ 0.59 GHz and ~ 6.3 GHz) correspond to the two lowest Lamb modes of the membrane. A 2D Fourier transform (1D spatial and 1D temporal) of the calculated displacement along the surface $u_x(0, y, t)$ reveals the dispersion relation of Lamb waves in the Al free-standing membrane. The result is shown in Fig. 4 and compared with the analytical solution of the Lamb wave dispersion relations [65, 66]. In the simulation, a

TABLE I. Best-fit parameter values on 400 nm Al free-standing membrane

Parameter	Explanation	Unit	Best-fit-value	lb[a]	ub[a]	Reference-value
G	electron-phonon coupling strength	$10^{16}\mathrm{Wm^{-3}K^{-1}}$	14	13.5	18.1	24.6 [59]
c_{l0}	longitudinal sound velocity	km/s	6.447	6.445	6.447	6.42 [60]
k_l	thermal conductivity	$\mathrm{Wm^{-1}K^{-1}}$	110	106	118	237 [60]
$\frac{\partial n}{\partial T}$	thermo-optic coefficient, real part	$-1\times10^{-3}\mathrm{K^{-1}}$	1.89	1.83	2.03	2.96–4.08[b]
$\frac{\partial \kappa}{\partial T}$	thermo-optic coefficient, imaginary part	$10^{-3}\mathrm{K^{-1}}$	2.62	2.16	2.8	0.4–4.4[b]
$\frac{dR}{RdT}$ [c]	thermoreflectance @ 800 nm	$10^{-4}\mathrm{K^{-1}}$	1.58	1.49	1.61	1.14–2.4 [61–63]

[a] The lower and upper bounds are determined by using a 5% $\Delta\chi^2$ criterion.
[b] The reference value on thermo-optic coefficient are determined by the optical conductivity data at varies temperatures in Ref. 64 together with available thermoreflectance data in Ref. 61–63.
[c] It is not a parameter used in the fit but is determined from the best-fit thermo-optic coefficient. Acoustic pulse central frequency $f_0 = 29.2$ GHz, FWHM bandwidth: $[8.6, 51.6]$ GHz.

source with small lateral dimension ($\sim$ 500 nm) is chosen to cover a wider k space. The model faithfully reproduces the analytical results. The expected frequencies of the first two lowest branches (at the transient grating wavenumber) are $\omega_{A_0} = 0.61$ GHz and $\omega_{S_0} = 5.5$ GHz.

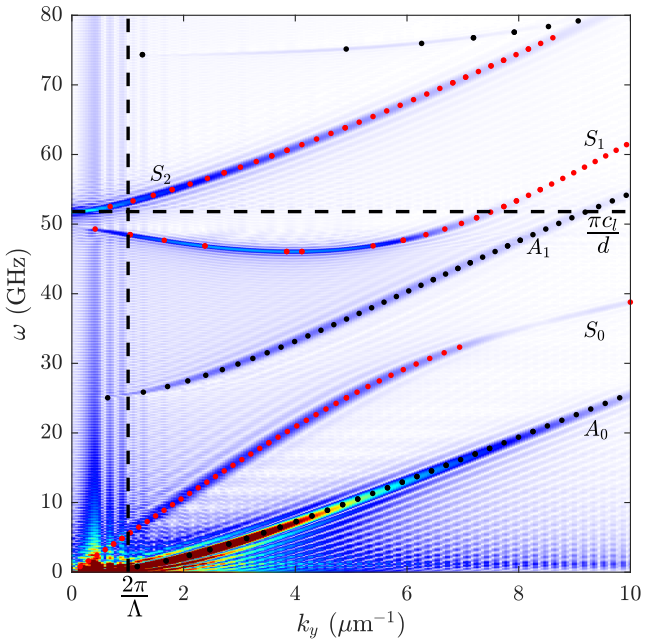

FIG. 4. Dispersion relation of Lamb waves in the Aluminium membrane retrieved from the simulation (color map). The black and red dots are the solution of the analytical expression of Lamb wave dispersion relations. Black dots correspond to asymmetric modes, and red dots to the symmetric modes. The vertical dashed line indicates the wave number of the transient grating used in the experiment, the horizontal dashed line indicates the round-trip frequency of longitudinal echoes.

Another intriguing aspect is the appearance of additional dips between the echoes, such as the one marked by the arrow at $t = 670$ ps in Fig. 3(a). Our model calculation suggests these dips are not longitudinal echoes, but actually result from mode conversion from longitudinal mode to higher order Lamb mode. Fig. 3(d) shows calculated surface displacement profiles at 3 time instants corresponding to the appearance of a longitudinal echo at $t = 608$ ps, the recovery of the echo event at $t = 640$ ps, and the appearance of the additional dip at $t = 670$ ps. As discussed before, the longitudinal echo is caused by a compensation of the TSE, therefore Fig. 3(d) shows a large difference between the dotted line and the solid line in the center of the grating line where the local optical intensity is maximal. However, as shown by the difference between the dashed line and the solid line, the additional dip is caused by a change of surface displacement in a region close to the periodic boundary where the optical intensity is minimal. In Fig. 3(e) we show the calculated surface displacement (in the direction of surface normal) at the periodic boundary (y=0) as a function of pump-probe delay. The timings of the additional dips are perfectly aligned with the dips in the surface displacement at y=0. This indicates that the origin of the additional dips is due to waves that are travelling along the surface, which results in constructive interference at the periodic boundaries. In thin free-standing membranes, these waves are a specific case of surface-guided waves called Lamb waves [65, 66]. The free boundary condition of membranes imposes that specific combinations of frequencies and wave numbers are allowed propagating waves while other combinations are evanescent. The dispersion relation shows a branch (S_2) starting at the round-trip frequency $\omega = \frac{\pi c_l}{d}$ of the longitudinal echoes, irrespective of the film thickness. This corresponds to the fundamental longitudinal vibration mode of the membrane. The longitudinal echo has a central frequency of $\frac{\pi c_l}{d}$, which naturally overlaps with this branch. Our present transient grating experiment can be seen as an effective excitation around the wave vector $k_y = \frac{2\pi}{\Lambda} = 1\ \mu\mathrm{m}^{-1}$, where $\Lambda = 6.24\ \mu$m is the transient grating period. Therefore, the longitudinal echoes effectively excite the S_2 branch at $k_y = 1\ \mu\mathrm{m}^{-1}$. Due to the diffraction of the longitudinal waves, part of the longitudinal echo arrives at the free boundary at an oblique angle, causing particle movement along the surface direction and converting some of its energy to the

S_2 Lamb wave mode every time it reaches the metal-air interface. From the dispersion relation, we calculate the phase velocity of the S_2 Lamb wave at $k_y = 1\ \mu\text{m}^{-1}$ as $v_{S_2} = 5.23 \times 10^4$ m/s. The time for the excited S_2 Lamb wave to travel across one period of the transient grating then is $\frac{\Lambda}{v_{S_2}} = 119.4$ ps, very close to the round-trip time of the longitudinal echoes $\frac{2d}{c_l} = 121$ ps. This agrees with the experimental observation that the period of the additional echoes appears the same as the longitudinal echoes. Thus the additional echoes can be explained as interference of S_2 Lamb waves at the periodic boundary which themselves are excited by mode conversion (longitudinal to Lamb mode). For small values of k_y, the slope of the S_2 branch on the determination of its phase velocity can be neglected, giving an approximation of $v_{S_2} = \frac{\pi c_l}{d} / \frac{2\pi}{\Lambda} = \frac{c_l \Lambda}{2d}$. Thus the predicted period of the additional echoes is $\frac{\Lambda}{v_{S_2}} = \frac{2d}{c_l}$, exactly the same as the round-trip time of the longitudinal echoes. This means that for small transient grating wavenumbers, the period of additional echoes is always the same (approximately) as the longitudinal echoes, irrespective with film thickness. This is also confirmed by simulations. The above analysis can also be used to understand the timing of the additional echoes to be in the middle of the longitudinal echoes. Since the above S_2 Lamb waves are excited at the moment when longitudinal echoes return to the surface, the time delay between the longitudinal echo and the time when the excited Lamb waves reaches the periodic boundary (and therefore interference maxima occurs) is $\Delta t = \frac{0.5\Lambda}{v_{S_2}}$, which is half of the longitudinal round-trip time. This means that there is a constant π phase delay between the appearance of the additional echoes and the longitudinal echoes. The growing amplitude of the additional echoes over time can be understood as an increasing mode conversion to the Lamb mode as more longitudinal reflections occur at the surface.

The fitting of model calculations to the experimental data was done with a "multi-start" procedure with 500 randomly generated initial parameter sets. The best-fit parameters and their comparison with reference values are summarized in Table I. By comparing different model fits, we found that acoustic attenuation was not significant for the present parameter range in aluminum, and conclude that the attenuation length far exceeds the measured acoustic propagation distance of $\sim 5\ \mu$m. The electron-phonon coupling strength of aluminium is about an order of magnitude larger than for gold [59]. This property of Al is correctly captured in the fitting result and the obtained value is somewhat lower than the reported DFT calculations [59]. Regarding the layer thickness, the sample specification gives an uncertainty smaller than 1 nm (d=391.1 nm), thus the thickness was fixed to this value during the fitting. As a result, the best-fit speed of sound has a very small uncertainty. Different from the case of gold as will be shown later, in which the measured data can be well-explained by contribution from only the surface displacement, the data of aluminum suggests a large contribution from the thermo-optic effect. This is to be expected, as the 800 nm probe wavelength coincides with the peak of the thermoreflectance spectrum of aluminum [63]. To determine the complex thermo-optic coefficient, we treat its real and imaginary parts as two extra fitting parameters. Their best-fit values are shown in Table I. From this thermo-optic coefficient, we then calculate the thermoreflectance using the Fresnel equation, resulting in a value of $\frac{dR}{RdT} = 1.58 \times 10^{-4}\ \text{K}^{-1}$, which lies well-within the range of other reported thermoreflectance data [61–63]. To the best of our knowledge, there is no direct report of the complex thermo-optic coefficient of aluminum in the literature, although the optical conductivity of Al measured at various temperatures is reported in Ref. 64. From this conductivity data together with the reported thermoreflectance data we then deduce the real and imaginary parts of the thermo-optic coefficient as reference values by inverting the Fresnel equation. Our best-fit coefficients are consistent with those deduced values. This demonstrates the ability to extract not only the thermoreflectance, but also the real and imaginary parts of the thermo-optic coefficient. It is worth noting that we have also measured the signal on a 100 nm Ni film on glass substrate, for which the detected signal also contains comparable contributions from surface displacement and the thermo-optic effect. The thermo-optic coefficient of Ni at 800 nm is of the opposite sign to that of Al [62], and this is again correctly captured in the material parameters retrieved from the Ni data, which are presented in the Supplemental Material [47].

In a short summary for Al, the signal we measured at 800 nm probing wavelength is a result of coherent sum of multiple physical effects, including surface displacement caused by thermal surface expansion and propagating longitudinal acoustic waves, mode conversion from longitudinal modes to higher order Lamb modes, interference of Lamb waves, and refractive index variation by the thermo-optic effect.

B. Measurements on gold films: complex hypersound attenuation behaviour

Transient grating experiments on gold were performed on two types of samples: a 500 nm Au layer deposited on a glass substrate and a 500 nm Au free-standing membrane. The measured data for both types of samples, along with the best-fit model results, are shown in Fig. 5(a-b). Strikingly different from the results of Al, fitting of the data of both gold samples reveals large contributions from acoustic attenuation. This behaviour requires an extension of the model to include the influence of microscopic damping mechanisms, as discussed below. At room temperature, the dominant mechanism for acoustic attenuation results from the interaction of acoustic phonons with thermal phonons [24, 25, 42, 67], a relaxational damping process that was first proposed by

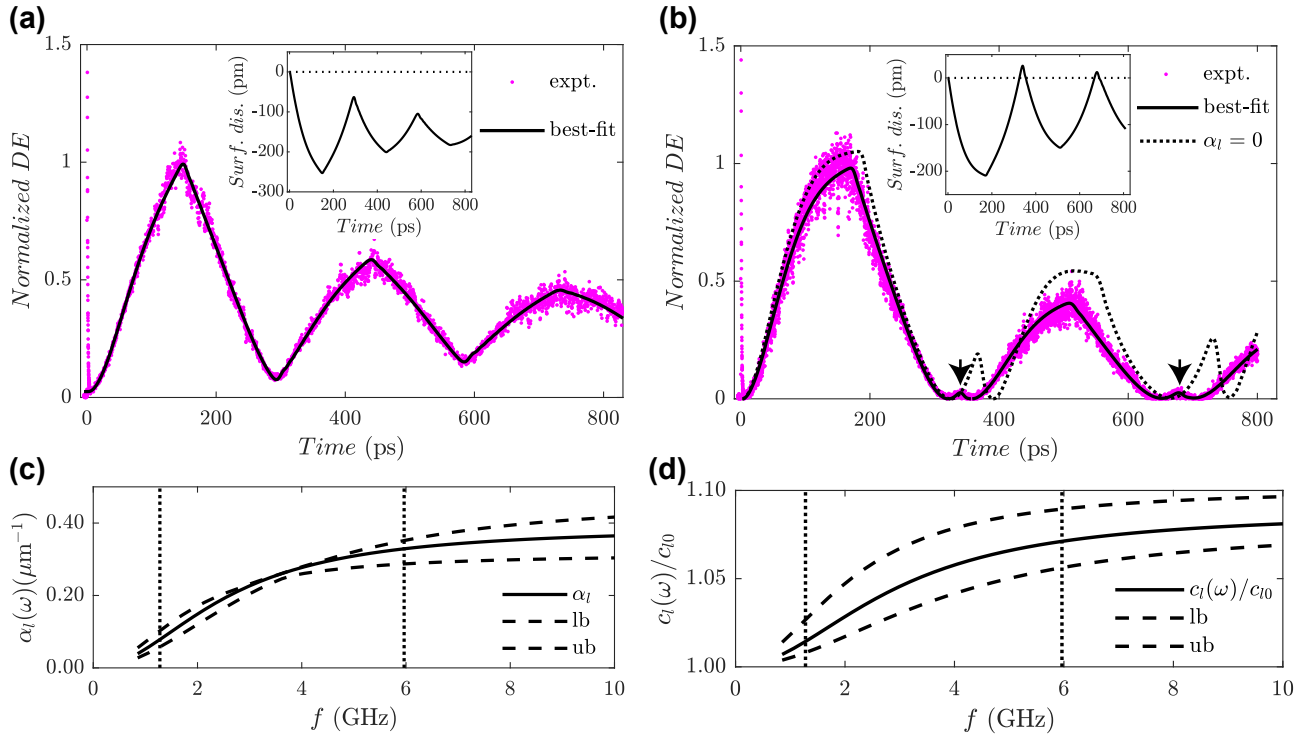

FIG. 5. Measured diffraction efficiency (dots) as a function of pump-probe delay and corresponding model fits (solid lines) on (a) 500 nm Au on glass substrate sample and (b) 500 nm Au free-standing membrane. The dotted-line in (b) is a calculation with no acoustic attenuation ($\alpha_l(\omega) = 0$). The insets are the calculated surface displacement at the center of the grating line. The dash-lines mark the level of zero surface displacement. (c) Frequency-dependent acoustic attenuation and (d) phase-velocity dispersion calculated by Eq. 9 and Eq. 10 using the best-fit parameters (solid lines). The dashed-lines are lower and upper bounds obtained from those fits with a 3% $\Delta\chi^2$ criterion. The vertical dotted-lines indicate the FWHM of the acoustic pulse bandwidth. Also see Video4 and Video5 in the Supplemental Material [47].

Akhiezer [68]. In this process, the sound waves disturb the distribution function of the thermal phonons, and the return of the system to equilibrium through phonon collisions removes the energy from the sound wave. The acoustic wave described by Eq. 6 exhibits viscous losses with quadratic power dependence on frequency, as it is the case in the Navier-Stokes equation. However, the Akhiezer damping mechanism can exhibit deviations from the quadratic power law, which has been observed in ultrafast laser induced hypersound waves [24, 25, 42]. Macroscopically, the Akhiezer damping manifests itself as a relaxation process originating from a noninstantaneous response of the medium to the change of the strain. An analogous effect in optics is the electromagnetic wave propagation in a lossy and dispersive medium, where the electric polarization density does not only depend on the electric field at the current time, but also on its values at all earlier times [51, 53]. To incorporate the relaxational Akhiezer damping into our model, we rewrite Eq. 6 as a convolution,

$$\sigma_x^v = -G_l(t) * [(\lambda_v + 2\xi)\frac{\partial s_x}{\partial t} + \lambda_v \frac{\partial s_y}{\partial t}],$$
$$\sigma_y^v = -G_l(t) * [(\lambda_v + 2\xi)\frac{\partial s_y}{\partial t} + \lambda_v \frac{\partial s_x}{\partial t}],$$
$$\sigma_{xy}^v = -G_s(t) * \xi \frac{\partial s_{xy}}{\partial t}, \qquad (7)$$

where $G_l(t)$ and $G_s(t)$ describe the relaxation process for the normal and shear waves, respectively. The functional form of $G_l(t)$ and $G_s(t)$ and the method for solving the convolutions are given in the Supplemental Material [47]. The attenuation $\alpha_l(\omega)$ for the Akhiezer damping is [25, 42, 69]

$$\alpha_l(\omega) = \frac{C_l T_l}{2\rho c_l(\omega)^3} \frac{\omega^2 \tau_l}{1 + \omega^2 \tau_l^2} (\langle \gamma^2 \rangle - \langle \gamma \rangle^2), \qquad (8)$$

where $c_l(\omega)$ the frequency-dependent longitudinal speed of sound, γ is the Grüneisen parameter of the thermal phonons, and τ_l is the longitudinal phonon relaxation time. The angular brackets stand for an average over the entire population of the thermal phonons. A similar expression also holds for the shear waves [70]. This expression can also be described by using a phenomenological

parameter, the bulk viscosity $\eta = C_l T_l \tau_l (\langle\gamma^2\rangle - \langle\gamma\rangle^2)$ as

$$\alpha_l(\omega) = \frac{\eta}{2\rho c_l(\omega)^3}\frac{\omega^2}{1+\omega^2\tau_l^2} = \alpha_{l0}(\frac{c_{l0}}{c_l})^3\frac{\omega^2}{1+\omega^2\tau_l^2}, \quad (9)$$

where we introduce the longitudinal speed of sound in the low frequency limit c_{l0} and $\alpha_{l0} = \eta/(2\rho c_{l0}^3)$. It is apparent that in the low frequency limit ($\omega\tau_l \ll 1$), $\alpha_l = \alpha_{l0}\omega^2$, Eq. 9 reduces to the quadratic power law. We show in the Supplemental Material [47] that the frequency-dependent attenuation exhibited by the model with the incorporation of Eq. 7 exactly reproduces the Akhiezer damping theory Eq. 9.

Because of the delayed response in Eq. 7, there must be associated acoustic dispersion, a requirement implied by causality: we find that the frequency-dependent phase velocity $c_l(\omega)$ exhibited by the model with the incorporation of Eq. 7 can be exactly described by the following expression

$$c_l(\omega) = c_{l0}(1 + \alpha_{l0}c_{l0}\frac{\omega^2\tau_l}{1+\omega^2\tau_l^2}). \quad (10)$$

It can be shown that Eq. 9 and Eq. 10 satisfy the Kramers-Kronig relations, and this is further discussed in the Supplemental Material [47]. In addition to dispersion and damping, the model can be extended to include acoustic nonlinearity by adding a quadratic term in the strain-stress relation. With the above expressions for attenuation and dispersion, the constitutive equations in one dimension reduce to the well-known Korteweg-de Vries-Burgers (KdVB) equation [19] when $\omega\tau_l \ll 1$, and this is derived in the Supplemental Material [47].

The obtained diffraction efficiency data in gold samples was fitted using the model with the incorporation of Eq. 7, starting with 200 random initial parameter sets. Important fitting parameters include the electron-phonon coupling constant, sound velocity, bulk viscosity, and the phonon relaxation time. The retrieved best-fit values are given in the Supplemental Material [47].

A comparison of the calculated diffraction efficiency using the best-fit parameters to the measured data is given in Fig. 5(a-b). As can be seen, the numerical calculations accurately reproduce the measurements. There are a few points worth mentioning in regards to these fits. Firstly, the electron response is not included in the model and therefore only the data points for $t > 10$ ps, when the electron gas has thermalized with the lattice, are used in the fits. Secondly, in contrast to the Al data, the contribution from surface displacement alone can explain the measured data very well. Thirdly, the sudden heating of the metal layer after electron-phonon thermalization gives rise to two effects: a thermal surface expansion (TSE) and the launch of an acoustic pulse. Both these effects lead to surface displacement and therefore both act as a phase grating seen by the probe pulse. For the 500 nm Au layer thickness, the spatial extent of the acoustic pulse is still too large to see a complete separation of the two contributions. The TSE manifests itself as a decaying background, because heat diffusion tends to reduce the surface-expansion. The traveling acoustic pulse, compensates the surface-expansion once every roundtrip time because of an opposite direction in the displacement vector: the reflected acoustic pulse arrives at the surface as a contraction instead of an expansion. For this reason, the acoustic echoes in Fig. 5(a) appears as dips in the diffraction signal. The situation is a bit different in the membrane sample as can be seen in Fig. 5(b), for which the echoes contain small bumps (marked by arrows) inside of large dips. This is because in the case of free-standing membrane, there is almost no reflection loss at material interfaces. As a results, the returning acoustic pulse is not only strong enough to fully compensate the (reduced) surface-expansion, but also change its direction (note the change of sign in the surface displacement plot). The height of this bump is largely determined by the amount of acoustic attenuation. In the unrealistic case of zero acoustic attenuation ($\alpha_l = 0$ of Fig. 5(b)), the bumps would be much more pronounced. We note that reflection losses at material interface due to scattering by roughness could be another mechanism for acoustic attenuation. Atomic force microscopy (AFM) was used to characterize the surface roughness of the gold films. While scattering is expected to be significant when the roughness size is comparable to the acoustic wavelength, the AFM data shows that the RMS roughness is only ~ 0.5 nm, well below the acoustic wavelength in the gold samples. In addition, the fit results of the 200 nm gold sample (Fig. 2(b)) suggest a very similar acoustic attenuation per unit propagation length as the 500 nm gold films. Considering the more frequent interface reflections (per propagation length) in the thinner sample, if the scattering loss dominates, the extracted acoustic attenuation per unit length would have been much larger. Due to these considerations, the scattering of acoustic waves at material interface is not considered further in our analysis.

The effect of acoustic dispersion can already be seen in Fig. 5(b) by the lower sound velocity (c_{l0}) in the dotted-line. The fitting yields the parameters α_{l0} and τ_l with which the frequency-dependent attenuation and phase-velocity dispersion can be obtained by evaluating Eq. 9 and Eq. 10. These quantities are plotted in Fig. 5(c-d). Rather than an ω^2-dependence expected for the low-frequency limit, the observed attenuation is even slower than ω^1. Using the best-fit parameter $\tau_l = 55$ ps and the central frequency of excited acoustic wave $f_0 = 2.77$ GHz in Au, we obtain $\omega_0\tau_l = 0.96$, indicating an intermediate regime $\omega\tau_l \sim 1$. It is worth noting that we have also performed a fit with a fixed $\tau_l = 1$ fs (thus $\omega\tau_l \ll 1$), forcing it to be in the frequency squared regime. In this case, we got a worse fit with almost twice the residual ($\chi^2 = 2.4$). This means that acoustic attenuation in this high frequency regime is better explained by relaxation damping, and incorporating such damping behaviour into

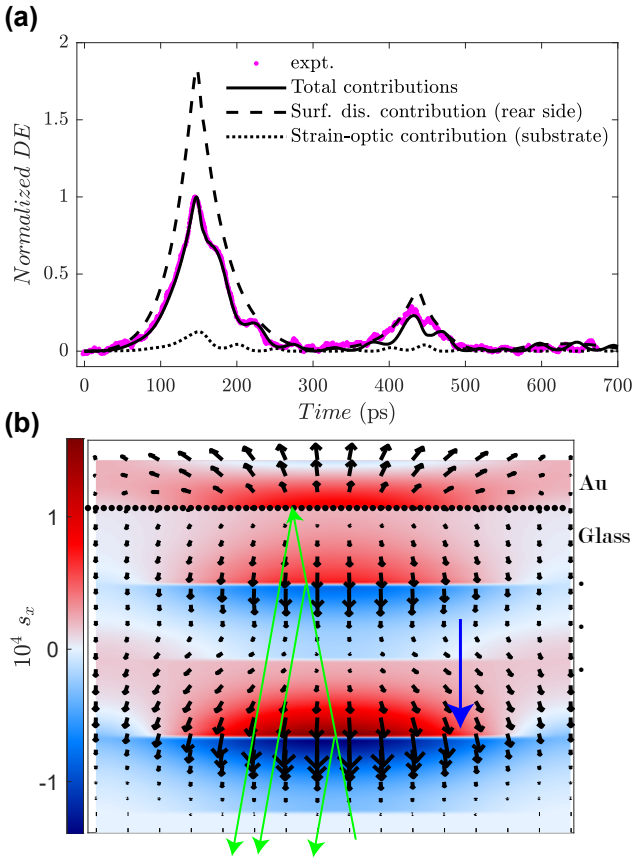

FIG. 6. (a) Measured diffraction efficiency (magenta dots) and the corresponding model calculation (solid line) on the 500 nm Au on glass sample pumped from the Au-Air side and probed at the Au-Glass interface. The diffraction efficiency (normalized by the maximum of the total contributions) calculated by only the displacement at the Au-Glass interface and by only the strain-optic effect in the glass substrate are shown as dash and dotted lines. The total contributions are a coherence addition of these two effects. (b) Strain (s_x component, color scale) and displacement vector distribution (black arrows) at $t = 582$ ps. Positive strain represents expansion while negative strain means compression. The filled-circles indicate the location of the Au-Glass interface. The blue arrow shows the propagation direction of the strain wave in glass. The green arrows illustrate the reflection of the probe pulse from the propagating strain pulses and the gold rear surface. Also see video 7 in the Supplemental Material [47].

the model improves the ability to model high frequency ultrasound attenuation in picosecond ultrasonic experiments.

The observed diffraction signal when probing from the air side does not contain a detectable contribution from the strain-optic effect. However, when we probe from the substrate (glass) side, the signal shows high frequency oscillations in addition to the expected surface displacement contribution. We attribute these additional oscillations to the strain-optic effect resulting from the acoustic wave propagation in the glass substrate. The generated acoustic pulse from the metal layer is partially transmitted into the substrate, resulting in a local expansion and compression of the glass, thus altering its refractive index. This strain wave forms additional gratings in the substrate, propagating at the speed of sound. The probe pulse then diffracts from both this moving strain wave and the substrate-metal interface, and these diffracted fields interfere constructively or destructively depending on the changing optical path difference. The overall effect is an oscillatory signal with a periodic given by $T = \frac{\lambda}{2nc_l cos(\theta)}$, where λ is the probe wavelength, n is the refractive index, c_l is the speed of sound in glass and θ is the angle of incidence. This effect known as Brillouin scattering is usually observed when performing reflectivity measurements [71–74]. In the present diffraction geometry, we observe a unique coherent addition of the Brillouin scattering and the surface displacement signal. Fig. 6(a) shows the measured diffraction efficiency and the model calculations when probing through the glass substrate side. In the calculations, we use the extracted parameters from the signal obtained when probing from the air side (Fig. 5(a)) and adjust the strain-optic coefficient of glass and the speed of sound in glass until a good match is found. The obtained values are $\frac{\partial n}{\partial s_x} = -0.35$ and $c_{gl} = 5.56$ km/s. In the experiments we use linearly polarized beam at normal incidence. Because the electric field vector of the probe beam is perpendicular to the propagation direction of the longitudinal acoustic wave, when the longitudinal strain is the only nonzero component, only the contribution from P_{12} of the photoelastic tensor is measured. Using the relation $P_{12} = -2\frac{\partial n}{\partial s_x}/n^3$ we obtain $P_{12} = 0.23$, in very good agreement with the reported value $P_{12} = 0.252$ [75].

As shown in Fig. 6(a), the signal shape and the detailed high frequency oscillations are well-reproduced, especially at early time delays. The strain-optic contribution here is calculated by using the simulated strain $s_x(x, y, t)$ and the transfer matrix method as explained in detail in the Supplemental Material [47]. The measured signal is a coherent addition of the displacement at the gold rear surface and the strain-optic effect caused by the acoustic wave propagation in the glass substrate. The slight mismatch after 400 ps may be due to the excitation of off-axis components (s_y and s_{xy}) as a result of acoustic diffraction. The off-axis components can introduce optical anisotropy and the probe may sample other elements of the photoelastic tensor. The displacement vectors at $t = 582$ ps as shown in Fig. 6(b) exhibit off-axis components in the region close to the periodic boundary. An extension of the probe calculation to include anisotropic media can further improve the results at longer time delays.

IV. SUMMARY

In this paper we have introduced a new approach to picosecond ultrasonics, which enables quantitative material characterization and the non-invasive study of opti-

cally opaque nanoscale materials using light-driven hypersound. We achieve this by introducing an advanced 2D numerical model that captures the generation, propagation and detection of these hypersound waves in full detail, and subsequently combining this model with measured data from picosecond ultrasonic experiments. By fitting the model to the experimental results, a detailed interpretation of the results in terms of the underlying physics is obtained, and a wide range of material properties is retrieved. To demonstrate this ability, we have demonstrated an simultaneous extraction of electron-phonon coupling constant, speed of sound, frequency-dependent acoustic attenuation and dispersion, and thermo-optic coefficients of several different materials as well as strain-optic constant with retrieved parameters that are consistent with literature values to the extent at which they were known. The extracted acoustic attenuation in gold films shows a frequency-dependency that deviates significantly from the quadratic power dependence, owing to enhanced relaxation damping in this high frequency range. In addition, we separate different contributions to the measured signal by simulations with the best-fit parameters. The results show large contributions of thermo-optic effects in Al and Ni and negligible contribution in Au at 800 nm probing wavelength. For aluminium, we identify the contributions of Lamb waves and mode conversion from longitudinal to Lamb waves, which are found to cause a gradual increase of the background level and additional dips at longer time delays. Furthermore, when probing from the glass side, we observe a unique coherent addition of the Brillouin scattering on top of the surface displacement signal which is well reproduced by simulations. Our model therefore holds great promise for disentangling various physical effects and interpreting signal formations in samples with complex geometries and advanced applications with surface nanotopographies and highly focused beams.

ACKNOWLEDGMENTS

This research was supported by the European Reseach Council (ERC Starting grant nr. 637476) and the Netherlands Organization for Scientific Research (NWO). This work was conducted at the Advanced Research Center for Nanolithography, a public-private partnership between the University of Amsterdam, Vrije Universiteit Amsterdam, the Netherlands Organization for Scientific Research (NWO), and the semiconductor-equipment manufacturer ASML.

[1] M. Maldovan, Sound and heat revolutions in phononics, Nature **503**, 209 (2013).
[2] T. Gorishnyy, C. K. Ullal, M. Maldovan, G. Fytas, and E. L. Thomas, Hypersonic phononic crystals, Phys. Rev. Lett. **94**, 115501 (2005).
[3] M. Oudich, M. Senesi, M. B. Assouar, M. Ruzenne, J.-H. Sun, B. Vincent, Z. Hou, and T.-T. Wu, Experimental evidence of locally resonant sonic band gap in two-dimensional phononic stubbed plates, Phys. Rev. B **84**, 165136 (2011).
[4] Y. Li and B. M. Assouar, Acoustic metasurface-based perfect absorber with deep subwavelength thickness, Appl. Phys. Lett. **108**, 063502 (2016).
[5] D. Xia, Z. Ku, S. C. Lee, and S. R. J. Brueck, Nanostructures and functional materials fabricated by interferometric lithography, Adv. Mater. **23**, 147–179 (2011).
[6] C. Thomsen, H. T. Grahn, H. J. Maris, and J. Tauc, Surface generation and detection of phonons by picosecond light pulses, Phys. Rev. B **34**, 4129 (1986).
[7] O. Matsuda, M. C. Larciprete, R. L. Voti, and O. B. Wright, Fundamentals of picosecond laser ultrasonics, Ultrasonics **56**, 3 (2015).
[8] H. Maris, Picosecond ultrasonics, Sci. Am. **278**, 86 (1998).
[9] B. C. Daly, N. C. R. Holme, T. Buma, C. Branciard, and T. B. Norris, Imaging nanostructures with coherent phonon pulses, Appl. Phys. Lett. **84**, 5180 (2004).
[10] K.-H. Lin, C.-T. Yu, S.-Z. Sun, H.-P. Chen, C.-C. Pan, J.-I. Chyi, S.-W. Huang, P.-C. Li, and C.-K. Sun, Two-dimensional nanoultrasonic imaging by using acoustic nanowaves, Appl. Phys. Lett. **89**, 043106 (2006).
[11] G. Tas and H. J. Maris, Electron diffusion in metals studied by picosecond ultrasonics, Phys. Rev. B **49**, 15046 (1994).
[12] O. B. Wright, Ultrafast nonequilibrium stress generation in gold and silver, Phys. Rev. B **49**, 9985 (1994).
[13] O. Matsuda, M. Tomoda, T. Tachizaki, S. Koiwa, A. Ono, K. Aoki, R. P. Beardsley, and O. B. Wright, Ultrafast ellipsometric interferometry for direct detection of coherent phonon strain pulse profiles, J. Opt. Soc. Am. B **30**, 1911 (2013).
[14] A. Devos and C. Lerouge, Evidence of laser-wavelength effect in picosecond ultrasonics: Possible connection with interband transitions, Phys. Rev. Lett. **86**, 2669 (2001).
[15] A. Devos and A. LeLouarn, Strong effect of interband transitions in the picosecond ultrasonics response of metallic thin films, Phys. Rev. B **68**, 045405 (2003).
[16] H.-Y. Hao and H. J. Maris, Experiments with acoustic solitons in crystalline solids, Phys. Rev. B **64**, 064302 (2001).
[17] O. L. Muskens and J. I. Dijkhuis, High amplitude, ultrashort, longitudinal strain solitons in sapphire, Phys. Rev. Lett. **89**, 285504 (2002).
[18] B. C. Daly, T. B. Norris, J. Chen, and J. B. Khurgin, Picosecond acoustic phonon pulse propagation in silicon, Phys. Rev. B **70**, 214307 (2004).
[19] P. J. S. van Capel and J. I. Dijkhuis, Time-resolved interferometric detection of ultrashort strain solitons in sapphire, Phys. Rev. B **81**, 144106 (2010).
[20] J.-W. Kim, M. Vomir, and J.-Y. Bigot, Ultrafast magnetoacoustics in nickel films, Phys. Rev. Lett. **109**, 166601 (2012).

[21] J. H. Lopes, M. A. B. Andrade, J. P. Leao-Neto, J. C. Adamowski, I. V. Minin, and G. T. Silva, Focusing acoustic beams with a ball-shaped lens beyond the diffraction limit, Phys. Rev. Applied **8**, 024013 (2017).

[22] B. Giammarinaro, D. Espindola, F. Coulouvrat, and G. Pinton, Focusing of shear shock waves, Phys. Rev. Applied **9**, 014011 (2018).

[23] S. Ayrinhac, M. Foret, A. Devos, B. Ruffle, E. Courtens, and R. Vacher, Subterahertz hypersound attenuation in silica glass studied via picosecond acoustics, Phys. Rev. B **83**, 014204 (2011).

[24] A. Devos, M. Foret, S. Ayrinhac, P. Emery, and B. Ruffle, Hypersound damping in vitreous silica measured by picosecond acoustics, Phys. Rev. B **77**, 100201(R) (2008).

[25] D. Li and D. G. Cahill, Attenuation of 7 ghz surface acoustic waves on silicon, Phys. Rev. B **94**, 104306 (2016).

[26] P. Emery and A. Devos, Acoustic attenuation measurements in transparent materials in the hypersonic range by picosecond ultrasonics, Appl. Phys. Lett. **89**, 191904 (2006).

[27] P. Ruello and V. E. Gusev, Physical mechanisms of coherent acoustic phonons generation by ultrafast laser action, Ultrasonics **56**, 21 (2015).

[28] V. V. Temnov, C. Klieber, K. A. Nelson, T. Thomay, V. Knittel, A. Leitenstorfer, D. Makarov, M. Albrecht, and R. Bratschitsch, Femtosecond nonlinear ultrasonics in gold probed with ultrashort surface plasmons, Nat. Commun. **4**, 1468 (2013).

[29] Q. Li, K. Hoogeboom-Pot, D. Nardi, M. M. Murnane, H. C. Kapteyn, M. E. Siemens, E. H. Anderson, O. Hellwig, E. Dobisz, B. Gurney, R. Yang, and K. A. Nelson, Generation and control of ultrashort-wavelength two-dimensional surface acoustic waves at nanoscale interfaces, Phys. Rev. B **85**, 195431 (2012).

[30] J. J. Kasinski, L. Gomez-Jahn, K. J. Leong, S. M. Gracewski, and R. J. D. Miller, Optical generation of coherent surface acoustics: an optically based probe of surface structure and dynamics, Opt. Lett. **13**, 710 (1988).

[31] A. M. Lomonosov, P. Hess, and A. P. Mayer, Observation of solitary elastic surface pulses, Phys. Rev. Lett. **88**, 076104 (2002).

[32] D. Nardi, M. Travagliati, M. E. Siemens, Q. Li, M. M. Murnane, H. C. Kapteyn, G. Ferrini, F. Parmigiani, and F. Banfi, Probing thermomechanics at the nanoscale: Impulsively excited pseudosurface acoustic waves in hypersonic phononic crystals, Nano Lett. **11**, 4126 (2011).

[33] C. Rossignol, J. M. Rampnoux, M. Perton, B. Audoin, and S. Dilhaire, Generation and detection of shear acousticwaves in metal submicrometric films with ultrashort laser pulses, Phys. Rev. Lett. **94**, 166106 (2005).

[34] Q. Xie, S. Mezil, P. H. Otsuka, M. Tomoda, J. Laurent, O. Matsuda, Z. Shen, and O. B. Wright, Imaging gigahertz zero-group-velocity lamb waves, Nat. Commun. **10**, 2228 (2019).

[35] T. F. Crimmins, A. A. Maznev, and K. A. Nelson, Transient grating measurements of picosecond acoustic pulses in metal films, Appl. Phys. Lett. **74**, 1344 (1999).

[36] T. Saito, O. Matsuda, and O. B. Wright, Picosecond acoustic phonon pulse generation in nickel and chromium, Phys. Rev. B **67**, 205421 (2003).

[37] O. Matsuda, O. B. Wright, D. H. Hurley, V. Gusev, and K. Shimizu, Coherent shear phonon generation and detection with picosecond laser acoustics, Phys. Rev. B **77**, 224110 (2008).

[38] R. M. Slayton, K. A. Nelson, and A. A. Maznev, Transient grating measurements of film thickness in multilayer metal films, J. Appl. Phys. **90**, 4392 (2001).

[39] C. He, O. Ristow, M. Grossmann, D. Brick, Y. Guo, M. Schubert, M. Hettich, V. Gusev, and T. Dekorsy, Acoustic waves undetectable by transient reflectivity measurements, Phys. Rev. B **95**, 184302 (2017).

[40] J. N. Hernandez-Charpak, K. M. Hoogeboom-Pot, Q. Li, T. D. Frazer, J. L. Knobloch, M. Tripp, S. W. King, E. H. Anderson, W. Chao, M. M. Murnane, H. C. Kapteyn, and D. Nardi, Full characterization of the mechanical properties of 11-50 nm ultrathin films: Influence of network connectivity on the poisson's ratio, Nano Lett. **17**, 2178 (2017).

[41] K. Naugolnykh and L. Ostrovsky, *Nonlinear Wave Processes in Acoustics* (Cambridge University Press, 1998).

[42] B. C. Daly, K. Kang, Y. Wang, and D. G. Cahill, Picosecond ultrasonic measurements of attenuation of longitudinal acoustic phonons in silicon, Phys. Rev. B **80**, 174112 (2009).

[43] S. Edward, H. Zhang, I. Setija, V. Verrina, A. Antoncecchi, S. Witte, and P. Planken, Detection of hidden gratings through multilayer nanostructures using light and sound, arXiv:1911.08337 [physics.app-ph] (2019).

[44] S. I. Anisimov, B. L. Kapeliovich, and T. L. Perelman, Electron emission from metal surfaces exposed to ultrashort laser pulses, Sov. Phys. JETP **39**, 375 (1974).

[45] T. Q. Qiu and C. L. Tien, Heat transfer mechanisms during short-pulse laser heating of metals, J. Heat Transfer **4**, 835 (1993).

[46] J. K. Chen and J. E. Beraun, Numerical study of ultrashort laser pulse interactions with metal films, Num. Heat Transfer, Part A **40**, 1 (2001).

[47] See Supplemental Material at [URL will be inserted by publisher] for a detailed description of the three-steps model, more discussions on the fitting procedure, the results on nickel, the extracted material parameters, the method to incorporate relaxitional damping, a derivation of the KdVB equation from our model and time evolution videos for all the samples in this paper.

[48] P. M. Shearer, *Introduction to Seismology* (Cambridge University Press, New York, 2009).

[49] R. D. Blandford and K. S. Thorne, *Applications of Classical Physics* (Stanford University and California Institute of Technology, 2013).

[50] J. H. Ferziger and M. Peric, *Computational Methods for Fluid Dynamics* (Springer, 2002).

[51] D. M. Sullivan, *Electromagnetic simulation using the FDTD method* (IEEE press, 2000).

[52] K. Yee, Numerical solution of initial boundary value problems involving maxwell's equations in isotropic media, IEEE Trans. Antennas Propag. **14**, 302 (1966).

[53] M. Born and E. Wolf, *Principles of Optics* (Cambridge University Press, Cambridge., 1999).

[54] S. Edward, A. Antoncecchi, H. Zhang, H. Sielcken, S. Witte, and P. C. M. Planken, Detection of periodic structures through opaque metal layers by optical measurements of ultrafast electron dynamics, Opt. Express **26**, 23380 (2018).

[55] J. Hohlfeld, S.-S. Wellershoff, J. Güdde, U. Conrad, V. Jähnke, and E. Matthias, Electron and lattice dynamics following optical excitation of metals, Chemical Physics **251**, 237 (2000).

[56] J. L. Hostetler, A. N. Smith, D. M. Czajkowsky, and P. M. Norris, Measurement of the electron-phonon coupling factor dependence on film thickness and grain size in Au, Cr, and Al, Appl. Opt. **38**, 3614 (1999).
[57] R. H. M. Groeneveld, R. Sprik, and A. Lagendijk, Femtosecond spectroscopy of electron-electron and electron-phonon energy relaxation in Ag and Au, Phys. Rev. B **51**, 11433 (1995).
[58] H. E. Elsayed-Ali, T. Juhasz, G. O. Smith, and W. E. Bron, Femtosecond thermoreflectivity and thermotransmissivity of polycrystalline and single-crystalline gold films, Phys. Rev. B **43**, 4488 (1991).
[59] Z. Lin, L. V. Zhigilei, and V. Celli, Electron-phonon coupling and electron heat capacity of metals under conditions of strong electron-phonon nonequilibrium, Phys. Rev. B **77**, 075133 (2008).
[60] D. R. Lide, *CRC Handbook of Chemistry and Physics, Internet Version 2005* (CRC Press, Boca Raton, FL, 2005).
[61] T.Favaloro, J.-H. Bahk, and A. Shakouri, Characterization of the temperature dependence of the thermoreflectance coefficient for conductive thin films, Rev. Sci. Instrum **86**, 024903 (2015).
[62] Y. Wang, J. Y. Park, Y. K. Koh, and D. G. Cahill, Thermoreflectance of metal transducers for time-domain thermoreflectance, J. Appl. Phys **108**, 043507 (2010).
[63] R. B. Wilson, B. A. Apgar, L. W. Martin, and D. G. Cahill, Thermoreflectance of metal transducers for optical pump-probe studies of thermal properties, Opt. Express **20**, 28829 (2012).
[64] A. G. MATHEWSON and H. P. MYERS, Optical absorption in aluminium and the effect of temperature, J. Phys. F: Metal Phys. **2**, 403 (1972).
[65] H. Lamb, On waves in an elastic plate, Proc. R. Soc. Lond. A. **93**, 114 (1917).
[66] J. L. Rose, *Ultrasonic Guided Waves in Solid Media* (Cambridge University Press, 2014).
[67] R. K. Singh and K. K. Pandey, Sound attenuation at high temperatures in pt, Acta Phys. Pol. a **109**, 219 (2006).
[68] A. Akhiezer, J. Phys (USSR) **1**, 277 (1939).
[69] T. Woodruff and H. Ehrenreich, Absorption of sound in insulators, Phys. Rev. **123**, 1553 (1961).
[70] S. K. Kor, U. S. Tandon, and G. Rai, Ultrasonic attenuation in copper, silver, and gold, Phys. Rev. B **6**, 2195 (1972).
[71] H. N. Lin, R. J. Stoner, H. J. Maris, and J. Tauc, Phonon attenuation and velocity measurements in transparent materials by picosecond acoustic interferometry, J. Appl. Phys. **69**, 3816 (1991).
[72] O. Matsuda, T. Pezeril, I. Chaban, K. Fujita, and V. Gusev, Time-domain brillouin scattering assisted by diffraction gratings, Phys. Rev. B **97**, 064301 (2018).
[73] A. Devos, R. Côte, G. Caruyer, and A. Lefèvre, A different way of performing picosecond ultrasonic measurements in thin transparent films based on laser-wavelength effects, Appl. Phys. Lett. **86**, 211903 (2005).
[74] V. E. Gusev and P. Ruello, Advances in applications of time-domain brillouin scattering for nanoscale imaging, Appl. Phys. Rev. **5**, 031101 (2018).
[75] A. Bertholds and R. Dandliker, Determination of individual strain-optic coefficients in single-mode optical fibers, J. Light. Technol. **6**, 17 (1988).